CHARLES E. SCHEMM, LAURENCE P. MANZI, and HARVEY W. KO

A PREDICTIVE SYSTEM FOR ESTIMATING THE EFFECTS OF RANGE- AND TIME-DEPENDENT ANOMALOUS REFRACTION ON ELECTROMAGNETIC WAVE PROPAGATION

A system of numerical models has been applied to the study of anomalous electromagnetic propagation in the lower atmosphere. The principal components of the system are a numerical model of the atmospheric boundary layer and APL's Electromagnetic Parabolic Equation code. The former predicts meteorological data at times and locations where measurements are not available. The latter takes estimates of refractivity obtained from the boundary-layer-model output and predicts propagation loss as a function of height and range. The system's usefulness is demonstrated by simulations of radar coverage anomalies.

INTRODUCTION

Radar coverage and communications are adversely affected by anomalous propagation (AP), which can occur as often as 95% of the time in some regions of the world.[1] AP is the abnormal bending and diversion of electromagnetic radiation from intended paths, resulting in problems with coverage fading, height errors, and anomalous clutter (Fig. 1).

AP is caused by nonstandard gradients of the atmospheric index of refraction (refractivity). As shown in Fig. 2, they fall into three general categories: subrefraction (abnormal bending up), superrefraction (abnormal bending down with a radius of curvature approaching that of the earth), and ducting or trapping (severe bending down with a radius of curvature much smaller than the earth's). Refractivity is a function of local temperature, pressure, and humidity.
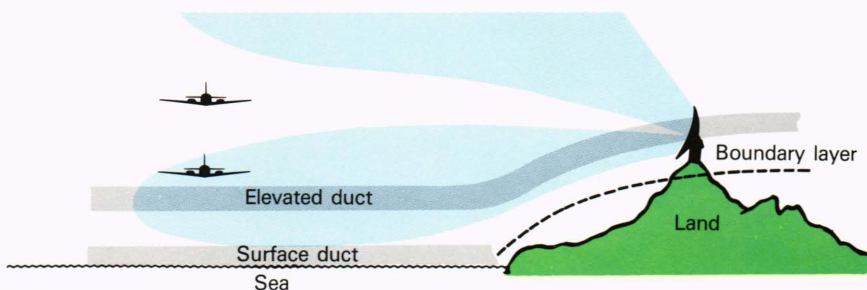
Antenna coverage patterns can be predicted using APL's Electromagnetic Parabolic Equation (EMPE) code,[1,2] which provides a physical optics solution for propagation loss in atmospheres described by inhomogeneous refractive-index changes and includes effects of diffraction and atmospheric absorption. Range-dependent refractivity gradients computed from the temperature, pressure, and humidity are used with EMPE to predict, for a specific antenna configuration, the expected propagation loss as a function of height, range, and time of day.

THE ROLE OF METEOROLOGICAL FORECASTING

The meteorological data required for EMPE calculations can be obtained in some cases from an instrumentation package called a radiosonde sent aloft by a balloon (Fig. 3). Unfortunately, however, the worldwide radiosonde network has neither the spatial nor the temporal resolution to describe quantitatively the evolution of refractive layers over scales at which the meteorological changes that affect radar performance are known to take place—typically 50 km and 1 to 3 hours. Radiosonde stations are spaced at approximately 500-km intervals in densely populated regions such as Europe and the continental United States. Over oceans and sparsely populated land masses (i.e., above 60°N and almost everywhere in the southern hemisphere), the spacing is much greater. Radiosondes are normally launched twice daily, at 0000 and 1200 UT, under the auspices of the World Meteorological Organization.

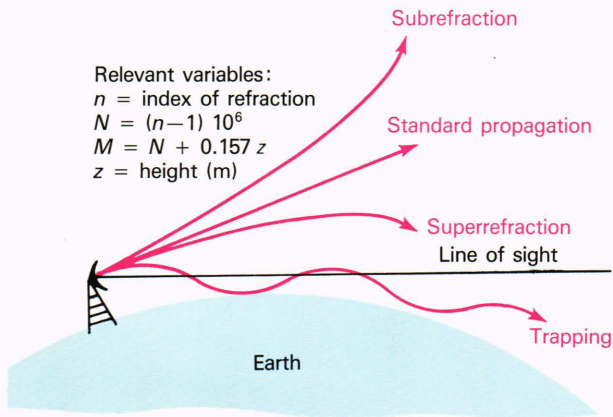Figure 1— Tactical implication of the sea breeze, boundary-layer modeling.

Relevant variables:
n = index of refraction
$N = (n - 1)\, 10^6$
$M = N + 0.157\, z$
z = height (m)

Subrefraction

Standard propagation

Superrefraction
Line of sight

Trapping

Earth

Figure 2—Examples of anomalous refraction.

The absence of meteorological data at scales of interest would severely hamper our ability to analyze a radar system's performance were it not for our ability to extrapo-

late data from one time and location to another by using a numerical model of the planetary boundary layer (PBL). The PBL is the lower portion of the atmosphere between the surface and the height at which the winds become independent of surface boundary conditions. This study demonstrates how EMPE and other propagation codes can be enhanced by using predictions from the boundary-layer model to provide meteorological and refractive-index data for range-dependent and time-varying situations.

Starting from measured atmospheric data at one location and time, the PBL model[3] in its most general form can predict data at locations and times for which no measurements are available. Predicted fields of temperature and humidity at selected times are used to estimate refractivity, vertical profiles of which are provided as input to EMPE. EMPE then predicts for a specified antenna configuration the expected radiation pattern as a function of height and range. The flow of data through the different components of the predictive system is illustrated in Fig. 4.
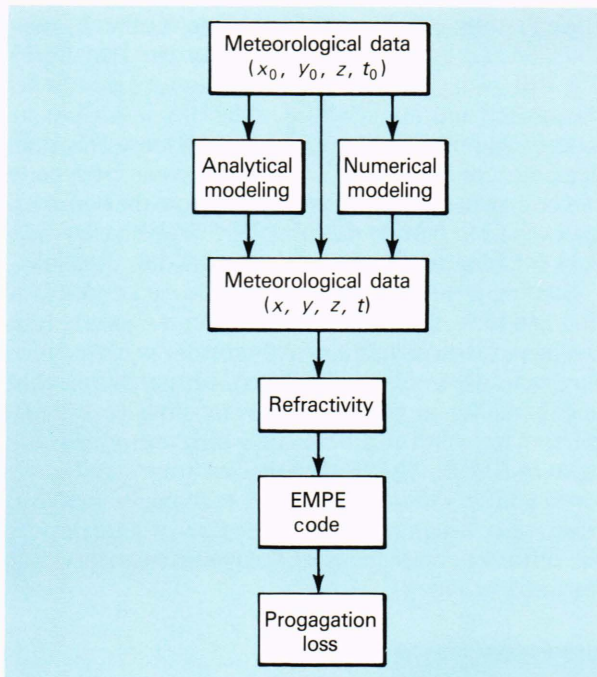

Figure 3—Radiosonde launch.

Figure 4—The data-collection, modeling, and analysis system.

As shown in the figure, numerical modeling is one of three possible options for obtaining space/time extrapolations of meteorological data. The first option, which is simply to use the nearest available measured data and to assume that they do not change over the time period and distances of interest, is not viable, as present results will show. The second option, which uses analytical (primarily scaling-law) models to obtain the desired space/time extrapolations, has enjoyed some success in horizontally homogeneous situations and in situations where the stratification does not change radically (e.g., from stable to unstable) during the forecast period. However, scaling laws require some a priori knowledge of parameters such as surface-layer stratification or height of the boundary layer. Such information is usually not available, except as output from a numerical model; for this reason the scaling-law approach is not generally suitable for forecasting purposes.

The potential of the model system outlined above to yield reliable predictions of the times and locations of ducting, surface clutter, and other manifestations of anomalous propagation is demonstrated by two case studies: one at a near-coastal desert site in the Mideast and the other near Roosevelt Roads, P.R. The first uses a one-dimensional time-dependent version of the PBL model and, in lieu of EMPE, the Integrated Refractive Effects Prediction System (IREPS) code[4] developed at the Naval Ocean Systems Center. The second case study uses a two-dimensional, steady-state version of the boundary-layer code to provide input to EMPE. The presence of a coastline in the Caribbean simulation provides a rigorous test of the model's capability in spatially inhomogeneous situations.

DESCRIPTION OF THE BOUNDARY-LAYER MODEL

The temporal evolution of temperature and humidity profiles in the lower atmosphere is predicted using the one-dimensional, time-dependent PBL model. The present version of the model solves differential equations for the horizontal wind velocity V, the potential temperature Θ, and the specific humidity, Q:

$$\frac{\partial U}{\partial t} = +f(V - V_g) + \frac{\partial}{\partial z}\left(K_m \frac{\partial U}{\partial z}\right), \quad (1)$$

$$\frac{\partial V}{\partial t} = -f(U - U_g) + \frac{\partial}{\partial z}\left(K_m \frac{\partial V}{\partial z}\right), \quad (2)$$

$$\frac{\partial \Theta}{\partial t} = \frac{\partial}{\partial z}\left(K_h \frac{\partial \Theta}{\partial z}\right) + S_\Theta, \quad (3)$$

$$\frac{\partial Q}{\partial t} = \frac{\partial}{\partial z}\left(K_h \frac{\partial Q}{\partial z}\right). \quad (4)$$

In the above equations, f is the Coriolis parameter, U_g and V_g are the x and y components of the upper level geostrophic wind, K_m and K_h are eddy coefficients of momentum and heat, respectively, and S_Θ is a radiative heating/cooling term to be discussed later. The principal assumptions leading to Eqs. 1 through 4 are the Boussinesq and hydrostatic approximations and an assumption of horizontal homogeneity. The latter enables us to neglect x and y derivatives in the original three-dimensional system of equations.

The potential temperature Θ is a normalized temperature defined as the temperature a parcel of air would assume if lowered adiabatically (i.e., without heat loss) to the surface. It is related to the measured temperature T by

$$\frac{\Theta}{T} = \left(\frac{P_{00}}{p}\right)^{R/c_p}, \quad (5)$$

where p is the atmospheric pressure and P_{00} is the surface pressure, here taken to be 1000 mb (1 mb = 100 Pa). $R = 287.04$ J/kg·deg is the gas constant, and $c_p = 1004.64$ J/kg·deg is the specific heat at constant pressure. In situations when moisture is important, it is more convenient to use the virtual potential temperature Θ_v defined by

$$\Theta_v = \Theta(1 + 0.608 Q). \quad (6)$$

The diffusion-like terms on the right side of Eqs. 1 through 4 are approximations to the turbulent transport terms that result when the original equations of motion are Reynolds averaged[5] to obtain mean-flow equations suitable for numerical integration. In the present model, the eddy coefficients K_m and K_h are evaluated using a nonlinear, stratification-dependent formulation described

396

as follows. For neutral and unstable stratification ($\partial \Theta_v / \partial z \leq 0$ locally), the eddy coefficients[6] are given by

$$K_m = K_h = (1 - 18\,Ri)^{1/2}\,l^2 S\,, \qquad (7)$$

where l is the turbulent mixing length, $S = [(\partial U / \partial z)^2 + (\partial V / \partial z)^2]^{1/2}$ is the local shear, and

$$Ri = \frac{g}{\Theta_0}\,\frac{\partial \Theta_v / \partial z}{(\partial U / \partial z)^2 + (\partial V / \partial z)^2}$$

is the gradient Richardson number. For the case of stable stratification ($\partial \Theta_v / \partial z > 0$), the eddy coefficients are written

$$K_m = K_h = \begin{cases} (1 - Ri/Ri_c)l^2 S & Ri < Ri_c \\ 0 & Ri > Ri_c \end{cases} \qquad (8)$$

with the critical Richardson number given by $Ri_c = 0.25$. The length scale l appearing in Eqs. 7 and 8 is evaluated[7] from

$$l = \frac{\kappa z}{1 + \kappa z / l_0} \qquad (9)$$

with the von Karman constant $\kappa = 0.35$ and the asymptotic length scale l_0 here set to 70 m.

The source term S_Θ in Eq. 3 accounts for direct radiative heating and cooling of the atmosphere. During daylight hours, the atmosphere is heated by incoming shortwave radiation that in the present model is determined by estimating the solar flux at the top of the atmosphere and reducing it at each level to account for absorption by water vapor.[8] The calculation of outgoing longwave radiation, which is responsible for much of the atmospheric cooling observed at night, is somewhat more complicated, involving both water vapor and CO_2. Our approach generally follows that of Mahrer and Pielke,[8] except that we have chosen not to make use of Sasamori's isothermal-atmosphere approximation.[9]

The equations of motion, Eqs. 1 through 4, are solved numerically on a grid that has the eddy coefficients K_m and K_h defined at half-grid intervals above and below the levels at which U, V, Θ, and Q are defined. The staggered-grid arrangement minimizes vertical averaging, which is detrimental to the accurate evaluation of vertical diffusion terms.

To provide increased resolution in the surface layer, the grid system is stretched in the vertical using[10,11]

$$\zeta = c_1 z + c_2 \ln\left(\frac{z + c_3}{c_3}\right)\,, \qquad (10)$$

where z is the physical height, ζ is the transformed height, and c_1, c_2, and c_3 are constants. The log-plus-linear transformation is appropriate for the planetary boundary layer because in most cases U, V, Θ, and Q vary approximately logarithmically with height near the surface, yet change much more slowly aloft. The physical heights of selected grid levels in the one-dimensional model are shown in Table 1.

Table 1 — Selected grid levels for U, V, Θ, and Q.

Level	z (m)	Level	z (m)
1	0	14	833.5
2	0.07	19	1251.6
3	4.13	24	1672.2
4	41.89	29	2094.0
5	107.78	34	2516.8
6	182.28	39	2940.1
7	260.27	44	3363.8
8	340.07	49	3787.9
10	502.65	51	3957.6
12	667.42	52	4042.4

The differential equations 1 through 4 are written in finite-difference form and integrated numerically using leapfrog or centered differencing. Viscous and diffusive terms, however, are treated implicitly so that the time step Δt may be set to a value larger than what would normally be required to satisfy the explicit viscous stability criterion

$$\Delta t \leq \frac{\Delta z^2}{4 K_m}\,. \qquad (11)$$

The finite-difference U-momentum equation, for example, is written

$$\begin{aligned} U_{n+1} = U_{n-1} &+ 2\Delta t\,\{f(V_k - V_g) \\ &+ \alpha[\delta_z(K_m\,\delta_z U)]_{n+1} \qquad (12) \\ &+ \beta[\delta_z(K_m\,\delta_z U)]_{n-1}\}\,, \end{aligned}$$

where subscript k refers to the vertical grid level and n is a measure of elapsed time in the numerical integration, $t = n\Delta t$. In the diffusion term, α and β are weights assigned to the forward and lag time-step components, respectively, and δ_z indicates a centered vertical difference. The tridiagonal matrix inversion required in the solution of Eq. 12 and in the comparable finite-difference equations for V, Θ, and Q is carried out using the standard Thomas algorithm for tridiagonal systems.[12]

Preliminary calculations using the one-dimensional model[13] have shown that oscillations tend to develop in the well-mixed layer below the temperature inversion when $\alpha = \beta = \frac{1}{2}$ and when the finite-difference time step is close to its (explicit) stability limit defined by Eq. 11. Therefore, like others,[14] we have chosen $\alpha = \frac{3}{4}$ and $\beta = \frac{1}{4}$. In addition, we have found that taking K_m at the lag time step ($n - 1$) in both terms of Eq.

12 is more effective in suppressing spurious oscillations than using K_m at n. The time-splitting instability inherent in leapfrog differencing is controlled by applying a time-smoothing filter after each iteration.[15]

At the top of the model ($z = H = 4$ km), we set $U = U_g$ and $V = V_g$ and require that $\partial\Theta/\partial z$ and $\partial Q/\partial z$ remain fixed at values determined from the initial measured vertical profiles of temperature and relative humidity. At the lower boundary, the no-slip condition ($U = V = 0$ at $z = z_0 \geq 0$) is realized by interpolating between levels 1 and 3 using similarity functions appropriate for the surface layer.[16] In this way, values of U and V at the $k = 2$ level are obtained that are needed in the solution of the momentum equations at $k = 3$. For Θ and Q, the procedure is similar except that the equations are complicated somewhat by the fact that temperature and humidity at z_0 vary with the time of day.

DIURNAL VARIATIONS AND ELECTRO-MAGNETIC WAVE PROPAGATION

The potential utility of the previously described PBL model in predicting changes in meteorological variables over time intervals that are important from the standpoint of radar propagation is demonstrated by a 12-hour time integration of the one-dimensional model equations 1 through 4, starting with measured data taken at a near-coastal desert site in the early morning of October 1, 1986. From measured values of temperature (Fig. 5a, far left profile) and relative humidity, the model varia-

bles Θ and Q were obtained using standard meteorological formulas.[17] Initial values of Θ and Q are shown in the far left profiles of Figs. 5b and 5c, respectively.

Wind speed and direction were not measured in this case but were obtained as functions of height by integrating the equations of motion in a diagnostic mode (temperature and humidity profiles fixed) while setting U and V at the top of the model equal to their seasonal averages. The latter data were available to us. The so-called "spin-up" process took 48 hours of simulated time.

The initial conditions and run parameters for the desert-site simulation are summarized in Table 2.

Figure 5 shows model predictions of temperature and humidity at hourly intervals for the 12-hour period between 0745 and 1945 LT on October 1. The initial temperature profiles (Figs. 5a, 5b, and 5d) show a temperature inversion at the surface as a result of nighttime

Table 2 — Parameters for the one-dimensional simulation.

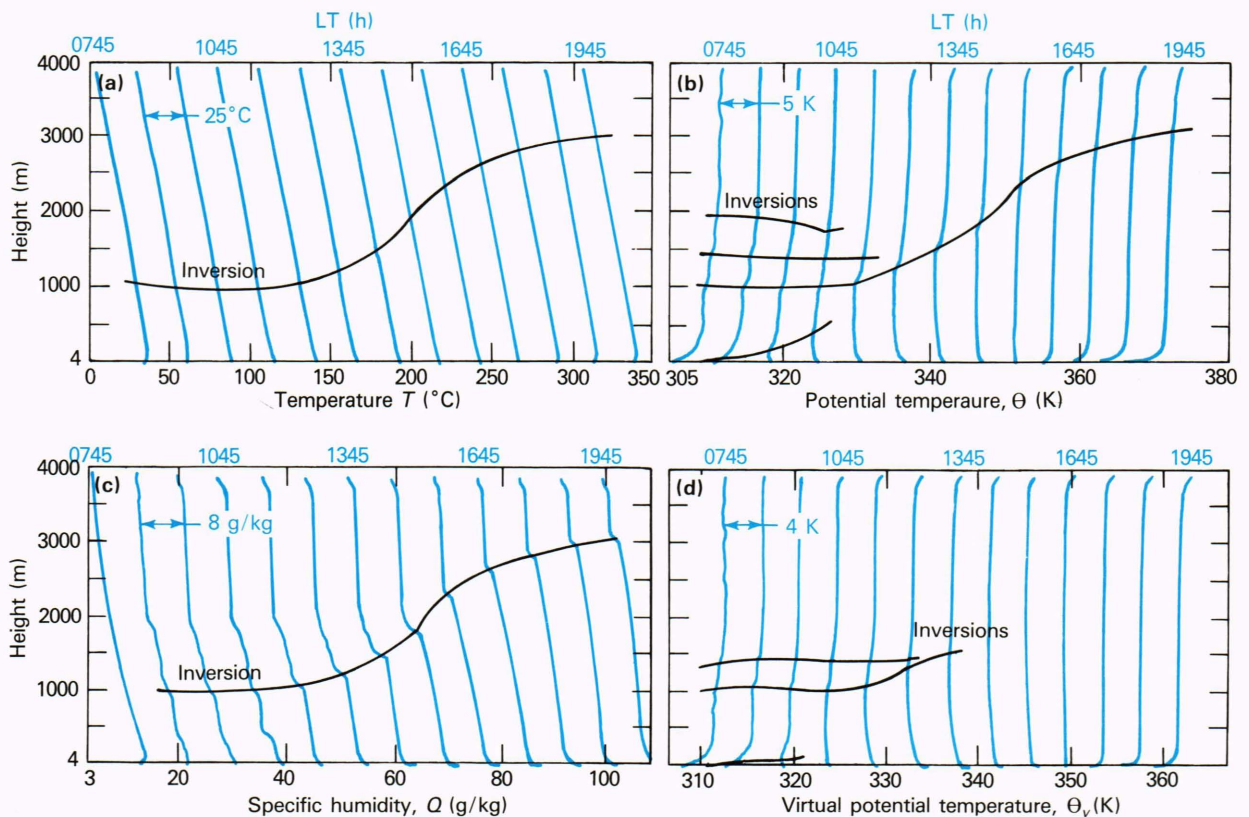|	
Latitude	$\phi = 26°16'$
Coriolis parameter	$f = 6.44 \times 10^{-5}$ s^{-1}
Geostrophic wind (x comp.)	$U_g = -1.91$ m/s
Geostrophic wind (y comp.)	$V_g = -4.62$ m/s
Roughness height	$z_0 = 0.01$ m
Height of model	$H = 4$ km
Number of interior grid levels	$k_{max} = 50$
Max. vertical grid spacing	$\Delta z_{max} = 84.9$ m
Time step	$\Delta t = 30$ s

Figure 5—Vertical profiles of meteorological variables from the desert-site simulation.

cooling and several weaker inversions between 1000 and 2000 m. As the ground is heated during the morning hours, the low-level inversion gradually erodes under the influence of thermal convection, disappearing entirely by 1145. At that point, the atmosphere is nearly adiabatic ($\partial \Theta_v / \partial z = 0$) between the ground and the mid-level inversion at 1200 m. The inversion continues to rise until late afternoon, when the surface begins to cool and thermal convection ceases.

The specific humidity profiles (Fig. 5c) show that water vapor is reasonably well mixed between the ground and the height of the lowest temperature inversion, with sharp drops in Q noted above each inversion. The virtual potential temperature profiles of Fig. 5d were obtained from Eq. 6 using predicted values of Θ and Q. For the most part, the Θ_v profiles are similar to the Θ profiles of Fig. 5b, with the notable exception that the mid-level inversion in Θ_v disappears sometime between 1345 and 1445, whereas a layer of positive $\partial \Theta / \partial z$ is evident throughout the calculation. The rather strong negative moisture gradient present at the mid-level inversion accounts for the difference.

Figure 6 shows the modified refractivity M as a function of height and time for the desert-site simulation. The far left M profile was obtained from measured temperature and humidity data at 0745 on October 1 using[18]

$$M = \frac{77.6}{T} \left(p - 4810 \frac{e}{T} \right) + 0.157 z . \quad (13)$$

In Eq. 13, T is the Kelvin temperature, p the atmospheric pressure in millibars, e the water-vapor pressure in millibars, and z the height in meters. Water-vapor pressure is obtained from T and Q by straightforward calculation. Subsequent M profiles were obtained from the model predictions of T and Q (Fig. 5), again using Eq. 13.

The 0745 data for M show a subrefractive layer ($dM/dz > 157$ km^{-1}) below about 100 m with normal conditions aloft. By 0845, however, the surface subrefractive layer has given way to a surface duct ($dM/dz < 0$), and superrefractive layers characterized by $0 < dM/dz < 79$ km^{-1} have formed at 350, 1050, and 2000 m. By 1045, an elevated duct has formed at 500 m, but it quickly disappears as what remains of the night-
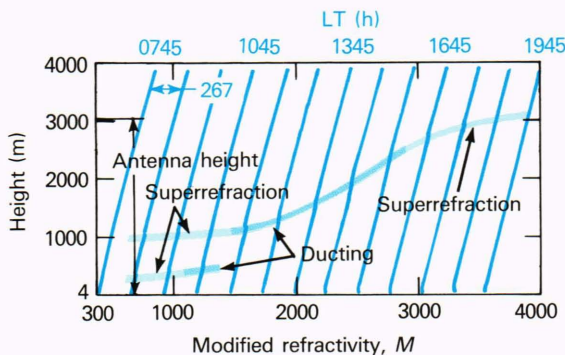
time stable layer is eroded by thermal convection. A second elevated duct forms between 1045 and 1145 from the superrefractive layer that was first seen at 0845 at the height of the mid-level temperature inversion, $z_i \approx 1050$ m (see Fig. 5b). It rises throughout the rest of the morning and the afternoon, tracking the mid-level inversion. By 1545, the inversion has reached 2400 m but has weakened to the extent that ducting is no longer observed. A residual superrefraction layer, however, persists to the end of the calculation, eventually rising above 3050 m, the height we have chosen for our hypothetical antenna. Changes in coverage patterns that might be expected under such circumstances are discussed below.

Changes in radar coverage in a vertically inhomogeneous, horizontally homogeneous atmosphere can be predicted using the IREPS code, which yields ray-trace-type coverage diagrams for a specified antenna system. For the present desert-site simulation, a hypothetical L-band antenna at 1.25 GHz is placed at 3050 m above mean sea level. The antenna has a vertical beamwidth of 4° and a −1.2° elevation.

Figure 7 shows predicted coverage diagrams for the desert site at selected local times between 0745 and 1945 on October 1. The patterns are similar to $(\sin x)/x$ with a free-space range of approximately 300 km. Since only direct rays from the antenna were predicted, there is no indication of surface reflections or multipath in the coverage diagrams.

At 0745, the antenna coverage is standard because the subrefractive layer is very close to the surface. At 0845, three coverage fades appear, caused by the three superrefractive layers at 350, 1050, 2000 m. The superrefraction continues to affect coverage adversely through 0945. The 1145 and 1345 diagrams show the coverage loss due
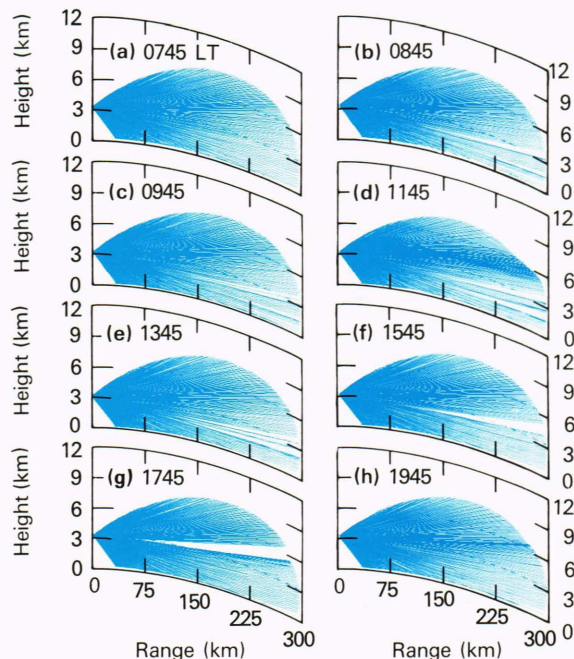

Figure 6—Refractivity profiles from the desert-site simulation.

Figure 7—IREPS propagation estimates for the desert site.

to the elevated duct rising from 1100 to 1500 m. The large coverage holes at 1545 and 1745 are due to the persistent superrefractive layer passing up through the antenna elevation. Clearly, the diurnal variation at the site causes dynamic changes in antenna coverage.

ELECTROMAGNETIC WAVE PROPAGATION IN A COASTAL ENVIRONMENT

The previously described PBL code has been reformulated as a two-dimensional, steady-state model and used to predict changes in meteorological variables across a land–sea interface. The equations of motion are similar to Eqs. 1 through 4 except that time-derivative terms have been neglected and, since the flow field is obviously not homogeneous in both horizontal dimensions, advective terms containing x derivatives (where the x axis is defined as perpendicular to the coastline) have been reintroduced. The resulting equations of motion are

$$U_0 \frac{\partial U}{\partial x} = + f(V - V_g) + \frac{\partial}{\partial z} \left(K_m \frac{\partial U}{\partial z} \right) , \quad (14)$$

$$U_0 \frac{\partial V}{\partial x} = - f(U - U_g) + \frac{\partial}{\partial z} \left(K_m \frac{\partial V}{\partial z} \right) , \quad (15)$$

$$U_0 \frac{\partial \Theta_v}{\partial x} = \frac{\partial}{\partial z} \left(K_h \frac{\partial \Theta_v}{\partial z} \right) , \quad (16)$$

and

$$U_0 \frac{\partial Q}{\partial x} = \frac{\partial}{\partial z} \left(K_h \frac{\partial Q}{\partial z} \right) , \quad (17)$$

which may be compared with Eqs. 1 through 4. Note that Eqs. 14 through 17 have been linearized by replacing the advective velocity U with the constant U_0. Note also that Θ_v is used in place of Θ in the heat-transfer equation and that the time-dependent radiation source/sink term that appeared in Eq. 3 does not appear in the present steady-state model.

Another difference between this and the previously described one-dimensional version of the boundary-layer code is that the lower boundary condition formulation is simplified somewhat by assuming that the atmosphere in the lowest few meters is unstratified. Under this assumption, the surface similarity functions reduce to logarithmic relationships of the form

$$\frac{|\mathbf{V}|}{u_*} = \frac{1}{\kappa} \ln \frac{z}{z_0} , \quad (18)$$

which may be applied between the surface and grid level 3 to evaluate both the friction velocity u_* and the variables U and V at level 2. The roughness height z_0 is fixed over land as before but is allowed to vary over water according to[19]

$$z_0 = \gamma u_*^2 / g , \quad (19)$$

with $\gamma = 0.016$.[20] In this case, the friction velocity u_* is determined by the simultaneous solution of Eqs. 18 and 19.

The two-dimensional model was initialized from a sounding taken at Roosevelt Roads, P. R., at 1030 LT on February 24, 1985, when the surface winds were blowing from the ESE at approximately 5 m/s. Consistent with the observed surface wind and with the measured temperature and humidity profiles is a southeast wind of 7.5 m/s aloft. In the absence of direct measurements of the upper level winds, we initially set $|\mathbf{V}| = |\mathbf{V}_g| = 7.5$ m/s everywhere above the first interior grid level.

The initial velocity field was allowed to spin up to a near steady state by integrating a diagnostic version of the one-dimensional time-dependent version of the boundary-layer code for 48 hours (slightly longer than one inertial period). After spin up, the two-dimensional equations were integrated in x to a location approximately 65 km NNW of Roosevelt Road (Fig. 8), where data were available for comparison. To allow for a smooth transition between land and maritime conditions, the surface temperature and humidity were changed linearly in a region extending roughly 1.5 km on either side of the coastline.

Table 3 summarizes the initial conditions and run parameters for the Caribbean simulation.

Figure 9 shows predictions of modified refractivity at approximately 5-km intervals between Roosevelt Roads and the location of the measurements. The first profile, calculated from the actual meteorological data at Roosevelt Roads, shows a weak elevated duct ($dM/dz < 0$) centered at approximately 75 m, topped by a superrefractive layer ($0 < dM/dz < 79$ km^{-1}) between 86 and 110 m. Superrefractive layers are also evident at 550 and 750 m. These features disappear 5 km downwind of Roosevelt Roads and are replaced by an elevated duct at the inversion level, $z_i \approx 950$ m, that persists throughout the calculation. A surface duct forms almost immediately and intensifies offshore as a consequence of lower temperatures and increased humidity at the sea surface. The surface duct is capped by a superrefractive layer, as shown in the figure.
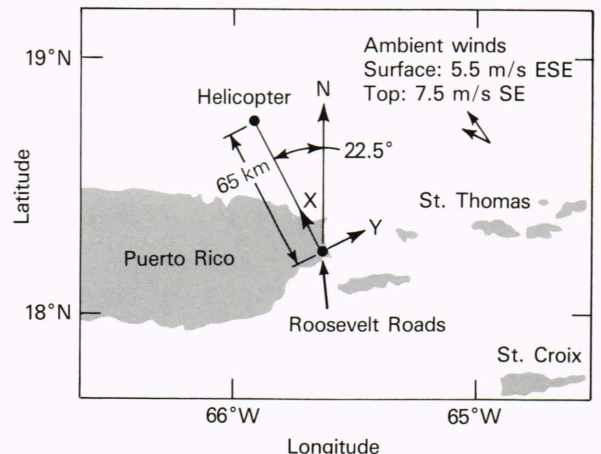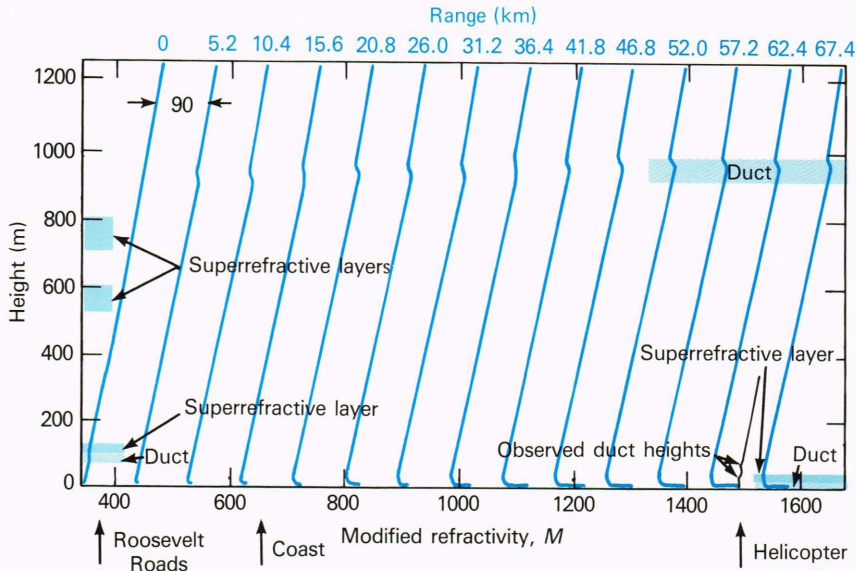

Figure 8—Two-dimensional model orientation.

Figure 9—Refractivity profiles from the Caribbean simulation.

Table 3 — Parameters for the two-dimensional simulation.

Latitude	$\phi = 18°20'$
Coriolis parameter	$f = 4.57 \times 10^{-5} \text{ s}^{-1}$
Geostrophic wind (x comp.)	$U_g = 6.93 \text{ m/s}$
Geostrophic wind (y comp.)	$V_g = 2.87 \text{ m/s}$
Surface temperature	$T_s = 27.2°C$ (land) $T_s = 24.0°C$ (water)
Surface humidity	$RH_s = 64\%$ (land) $RH_s = 100\%$ (water)
Roughness height	$z_0 = 0.01 \text{ m}$ (land)
Height of model	$H = 1.25 \text{ km}$
Number of interior grid levels	$k_{max} = 50$
Max. vertical grid spacing	$\Delta z = 26.4 \text{ m}$
Horizontal domain	$L = 67.6 \text{ km}$
Spatial increment	$\Delta x_{max} = 52 \text{ m}$
Number of spatial iterations	$N = 1300$

Figure 10—Predicted antenna coverage for an inhomogeneous atmosphere determined from the boundary-layer simulation (Fig. 9).

Figure 9 also shows a profile of modified refractivity obtained from meteorological data taken with an instrumented helicopter[21] stationed approximately 65 km NNW of Roosevelt Roads. These data were taken at 0928 LT on February 24, 1985, and for all practical purposes are coincident with the land-based radiosonde data from Roosevelt Roads. The significant features in the measured refractivity data (second profile from the right on Fig. 9) are a surface duct below 25 m and an elevated duct between 50 and 60 m.

The PBL model predicts the observed surface duct almost exactly, but the elevated duct and the subrefractive layer below it appear in the model output as a single superrefractive layer, presumably the result of the model's relatively poor vertical resolution. Helicopter measurements are capable of providing finer resolution data ($\Delta z \approx 3m$) than can be obtained from standard radiosonde measurements. In this case, the helicopter did not

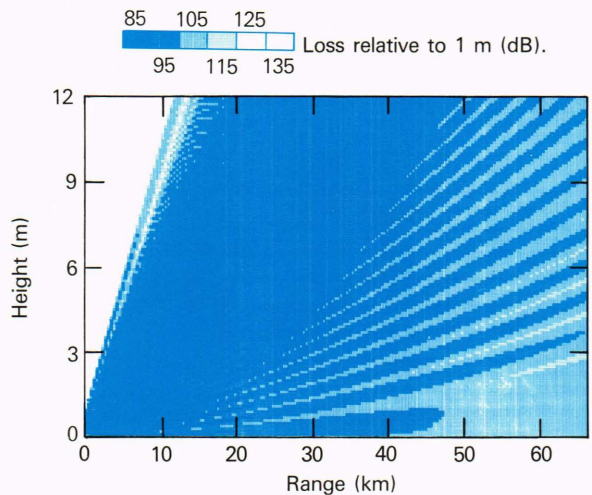profile high enough in the atmosphere to confirm the presence of the elevated duct at 950 m.

A case study for hypothetical S-band propagation in the coastal environment is possible using APL's EMPE code which, unlike IREPS, can accommodate a horizontally inhomogeneous atmosphere. In addition, EMPE can provide propagation losses near the surface accounting for diffraction as well as refraction. Figure 10 is the EMPE result for propagation loss for an S-band antenna ($f = 3$ GHz) under spatially inhomogeneous atmospheric conditions predicted by the PBL model. The hypothetical antenna is placed 30 m above sea level at Roosevelt Roads and is horizontally polarized with a 3° vertical beamwidth and a +1.5° elevation angle. The gray scale gives one-way propagation loss in decibels relative to 1 m from the antenna in increments of 10 dB.

Figure 10 shows energy being trapped and guided onto the surface over the entire range, leading to excessive

over-the-horizon clutter. The trapping is caused by the formation of the evaporative duct over water (Fig. 6). At Roosevelt Roads, the elevated duct is above the antenna and, hence, has little effect on propagation.

The results for an inhomogeneous atmosphere may be compared with those of Fig. 11 for a spatially homogeneous atmosphere in which the measurements at Roosevelt Roads are assumed to apply over water as well. Since the antenna is always beneath the duct under homogeneous conditions, only slight ducting is evident downrange between 35 and 65 km, where electromagnetic rays eventually couple to the elevated duct. The obvious benefit is the ability to describe the true, horizontally inhomogeneous situation and not having to rely on a single-profile, horizontally homogeneous assumption.

SUMMARY

A system of numerical models has been developed that can provide predictions of anomalous propagation between one location and time where meteorological data would normally be available, and a second location and time where the required meteorological data may not be available. The first component of the system is APL's planetary boundary-layer model, either the one-dimensional, time-dependent version used for the desert-site simulation or the two-dimensional, steady-state version used for the Caribbean simulation. The second major component is an electromagnetic wave propagation code, either IREPS or EMPE.

The boundary-layer models accept as input temperature and relative-humidity data in the form that would normally be provided by routine meteorological soundings. They return estimates of temperature, humidity, and refractivity at later times and at locations downwind of the point where the initial data are provided. The PBL models can predict small-scale features (e.g., temperature inversions) that can cause anomalous propagation. Refractivity data as a function of range and height are then provided either to IREPS or to EMPE, which return estimates of propagation loss, including coverage voids and
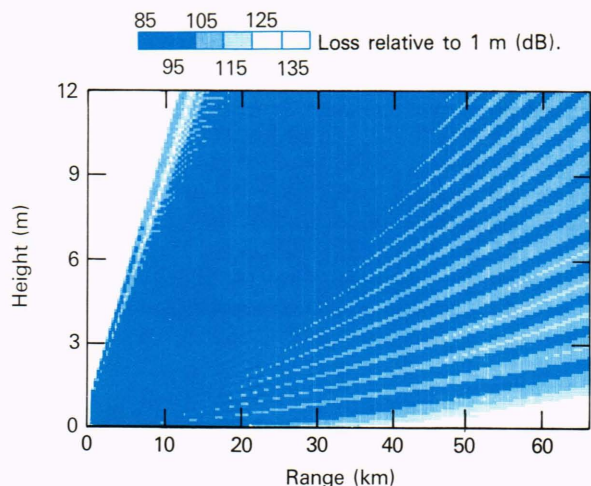

Figure 11—Predicted antenna coverage for a homogeneous atmosphere based on data from Roosevelt Roads.

areas of expected clutter. Output from propagation codes is used in the analysis of instances of anomalous propagation and in attempts to predict how often and under what conditions anomalous propagation can be expected at a given antenna site.

Applicability of the present modeling system is generally restricted to physical situations where the assumptions and approximations associated with the planetary boundary-layer model are not violated. The primary requirement for application of the one-dimensional model is that the atmosphere be horizontally homogeneous, which precludes its use in coastal environments. For the two-dimensional steady-state model, the mean wind must be nearly steady and blowing generally in the direction of interest. The latter condition can be relaxed somewhat if there are no land–sea interfaces, terrain changes, or other spatial inhomogeneities in the transverse or y direction. The criteria were easily met in the simulations discussed here, where the geostrophic wind was blowing at 22.5° relative to the x axis in the coordinate system of Fig. 8.

In other situations, however, especially in coastal regions, the mean-wind forcing may be weak compared with the thermal forcing associated with differential heating at the land–sea interface. Differential heating gives rise to land and sea breezes, mesoscale phenomena that can result in the surface winds blowing opposite to the mean upper level winds at certain times of the day and over distances within, say, 100 km of the coastline. In such cases, steady-state modeling is not applicable, and a full two-dimensional, time-dependent model must be used. Such a model is under development at APL.

Other potential deficiencies in the PBL models described here are the absence of condensation and evaporation processes and the use of a first-order, eddy-viscosity turbulence closure scheme (Eqs. 7 through 9). The former problem could cause serious errors in predictions for locations where clouds are present; this problem has been corrected in the most recent version of the code by adding a cloud-physics parameterization scheme similar to that proposed by Sommeria and Deardorff[22] and Mellor.[23] Although it does not appear to have affected predictions of gross features in the boundary layer, the present simplified turbulence formulation may be causing errors in some of the smaller scale features in temperature and humidity, especially in the surface layer. If subsequent comparisons with data show this to be the case, it may be necessary to replace the present scheme with a more sophisticated second-order closure formulation.[7,24]

REFERENCES

[1]H. W. Ko, J. W. Sari, M. E. Thomas, P. J. Herchenroeder, and P. J. Martone, "Anomalous Propagation and Radar Coverage through Inhomogeneous Atmospheres," presented at the 33rd Symposium, Electromagnetic Wave Propagation Panel, NATO Advisory Group for Aerospace Research and Development, Spatind, Norway (Oct 4–7, 1983).

[2]H. W. Ko, J. W. Sari, and J. P. Skura, "Anomalous Microwave Propagation through Atmospheric Ducts," *Johns Hopkins APL Tech. Dig.* **4**, 12–26 (1983).

[3]C. E. Schemm and L. P. Manzi, "Computer Simulations of Changes in Radar Refractivity in the Lower Atmosphere," in *Proc. 1987 Summer Computer Simulations Conf.*, pp. 295–300 (1987).

[4]H. V. Hitney and R. A. Paulus, *Integrated Refractive Effects Prediction Sys-*

tem (*IREPS*), *Interim Users Manual,* TD 238, Naval Ocean Systems Center, San Diego (1979).

[5]A. S. Monin and A. M. Yaglom, *Statistical Fluid Mechanics,* J. L. Lumley, ed., MIT Press, pp. 205–264 (1971).

[6]A. K. Blackadar, "High Resolution Models of the Planetary Boundary Layer," *Adv. Environ. Sci. Eng.* **I**, 50–85 (1979).

[7]G. L. Mellor and T. Yamada, "A Hierarchy of Turbulence Closure Models for Planetary Boundary Layers," *J. Atmos. Sci.* **31**, 1791–1806 (1974).

[8]Y. Mahrer and R. A. Pielke, "The Effects of Topography on Sea and Land Breezes in a Two-Dimensional Numerical Model," *Mon. Weather Rev.* **105**, 1151–1162 (1977).

[9]T. Sasamori, "A Linear Harmonic Analysis of Atmospheric Motion with Radiative Dissipation," *J. Meteorol. Soc. Japan* **50**, 505–517 (1972).

[10]T. Yamada and G. Mellor, "A Simulation of the Wangara Atmospheric Boundary Layer Data," *J. Atmos. Sci.* **32**, 2309–2329 (1975).

[11]T. Yamada, "An Application of a Three-Dimensional, Simplified Second-Moment Closure Numerical Model to Study Atmospheric Effects of a Large Cooling Pond," *Atmos. Env.* **13**, 693–704 (1979).

[12]R. D. Richtmyer and K. W. Morton, *Difference Methods for Initial Value Problems,* 2nd ed., Interscience, pp. 178–201 (1967).

[13]C. E. Schemm, L. P. Manzi, and D. A. Roberts, "Planetary Boundary Layer Modeling Applied to Anomalous Propagation Studies," *Bull. Am. Phys. Soc.* **31**, p. 1711 (1986).

[14]J. Paegle, W. G. Zdunkowski, and R. M. Welch, "Implicit Differencing of Predictive Equations of the Boundary Layer," *Mon. Weather Rev.* **104**, 1321–1324 (1976).

[15]R. Asselin, "Frequency Filter for Time Integrations," *Mon. Weather Rev.* **100**, 487–490 (1972).

[16]J. A. Businger, "Turbulent Transfer in the Atmospheric Surface Layer," in *Workshop on Micrometeorology,* D. A. Haugen, ed., American Meteorological Society, pp. 67–100 (1973).

[17]A. E. Gill, *Atmosphere-Ocean Dynamics,* Academic Press, New York (1982).

[18]B. R. Beam and E. J. Dutton, *Radio Meteorology,* Dover, New York (1968).

[19]H. Charnock, "Wind Stress on a Water Surface," *Q. J. R. Meteorol. Soc.* **81**, 638–640 (1955).

[20]J. Wu, "Wind Stress and Surface Roughness at Air-Sea Interface," *J. Geophys. Res.* **74**, 444–455 (1969).

[21]S. M. Babin, J. R. Rowland, and J. H. Meyer, *Results of Meteorological Measurements from the February 1985 Puerto Rico Experiment,* JHU/APL SIR-85U-025 (1985).

[22]G. Sommeria and J. W. Deardorff, "Subgrid-Scale Condensation in Models of Nonprecipitating Clouds," *J. Atmos. Sci.* **34**, 344–355 (1977).

[23]G. L. Mellor, "The Gaussian Cloud Model Relations," *J. Atmos. Sci.* **34**, 356–358 (1977).

[24]G. L. Mellor and T. Yamada, "Development of a Turbulence Closure Model for Geophysical Fluid Problems," *Rev. Geophys. Space Phys.* **20**, 851–875 (1982).

THE AUTHORS
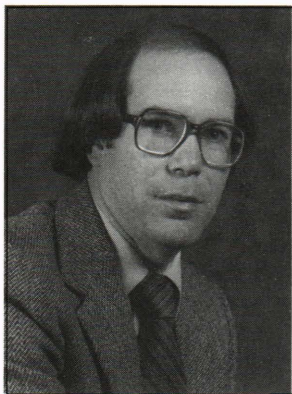
CHARLES E. SCHEMM was born in Baltimore in 1947. He received a B.S. degree in physics from Loyola College in 1969 and a Ph.D. in geophysical fluid dynamics from Princeton University in 1974. He became a research associate (1974–77) at what is now the Institute for Physical Science and Technology of the University of Maryland, where he subsequently was visiting lecturer in the Meteorology Department (1977–81).

Since joining APL in 1977, Dr. Schemm has been involved in planning and conducting ocean experiments and in the numerical modeling of oceanic and atmospheric phenomena, most recently involving the earth's planetary boundary layer. His research interests include turbulence modeling, small- and intermediate-scale ocean dynamics, mesoscale meteorology, and boundary layers. He is supervisor of the Ocean Science Section in the Hydrodynamics Group.
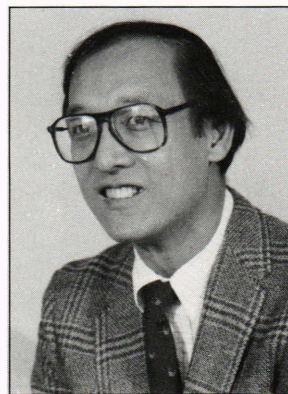
HARVEY W. KO was born in Philadelphia in 1944 and received the B.S.E.E. (1967) and Ph.D. (1973) degrees from Drexel University. During 1964–65, he designed communications trunk lines for the Bell Telephone Company. In 1966, he performed animal experiments and spectral analysis of pulsatile blood flow at the University of Pennsylvania Presbyterian Medical Center.

After joining APL in 1973, he investigated analytical and experimental aspects of ocean electromagnetics, including ELF wave propagation and magnetohydrodynamics. Since 1981, he has been examining radar wave propagation in coastal environments, advanced biomagnetic processing for encephalography, and brain edema. He is now a member of the Submarine Technology Department staff.

LAURENCE P. MANZI was born in Philadelphia in 1941 and received a B.S. degree in physics from Rensselaer Polytechnic Institute in 1963 and an M.S. degree from Northeastern University in 1965. He was an instructor in physics at West Liberty State College and was a research assistant at the Educational Policy Research Center in Washington, D.C., before joining Sachs/Freeman Associates in 1978. He has provided programming support to scientists in APL's Hydrodynamics Group on a number of projects, most recently the analysis of GEOSAT altimeter data and the numerical modeling of the atmospheric planetary boundary layer.